Journal of Materials Science & Technology 211 (2025) 171–178

Contents lists available at ScienceDirect

Journal of Materials Science & Technology

journal homepage: www.elsevier.com/locate/jmst

Research Article

Abnormally enhanced displacement burst at elevated temperatures of AZ31 magnesium alloy during nanoindentation

Song-Yu Yan[a], Zhang-Jie Wang[b,*], Zhi-Wei Shan[a,*]

[a] Center for Advancing Materials Performance from the Nanoscale (CAMP-Nano), State Key Laboratory for Mechanical Behavior of Materials, Xi'an Jiaotong University, Xi'an 710049, PR China
[b] Center for Alloy Innovation and Design (CAID), State Key Laboratory for Mechanical Behavior of Materials, Xi'an Jiaotong University, Xi'an 710049, PR China

ARTICLE INFO

Article history:
Received 23 February 2024
Revised 10 May 2024
Accepted 11 May 2024
Available online 14 June 2024

Keywords:
Nanoindentation
Pop-in
Gaussian-like distribution
Dislocation nucleation
Prismatic slip

ABSTRACT

The unveiling of temperature effects on the deformation behaviors of wrought magnesium (Mg) alloys is beneficial for optimizing the hot forming parameters of these alloys with limited room temperature (RT) formability. In the present work, we performed nanoindentations on individual grains of textured wrought AZ31 alloy along the normal direction (ND) from RT to 300 °C to investigate the intrinsic non-basal dislocation behaviors at various temperatures. Interestingly, we observed abnormally enhanced nanoindentation displacement bursts (pop-ins) at elevated temperatures ranging from 150 to 250 °C, which is beyond the general scenario that higher temperatures typically result in smoother plastic flow. The bursts exhibited Gaussian-like statistics, which differ from the well-reported bursts with power-law size distributions resulting from the destruction of jammed dislocation configurations. Through transmission electron microscopy (TEM) examination of the microstructure beneath the indentation just after the burst, we found that the abnormal displacement bursts originated from the heterogeneous nucleation of prismatic screw ⟨**a**⟩ dislocations due to the exhaustion of dislocation sources within the specified temperature range.

1. Introduction

Magnesium (Mg) alloys are promising candidates for weight-sensitive applications in digital products, vehicle engineering, aerospace, and other fields [1,2] due to low density and high specific strengths [3,4]. Generally, cast Mg alloys have prevalent defects, such as casting porosity, cracks, element segregation, and grain coarsening. These casting defects can be eliminated by extrusion, rolling, forging, and other forming treatments. As a result, the microstructure of wrought Mg alloys becomes more compact, uniform, and refined, leading to higher strength and improved ductility [5].

However, during plastic forming at room temperature (RT), Mg alloys crack easily due to the von Mises criterion, which requires five independent slip systems for intergranular strain compatibility in polycrystalline materials, cannot be fulfilled [6,7]. The most easily operated basal ⟨**a**⟩ slip can only offer two independent modes within the basal plane. In addition to dislocation slip, RT deformation by tensile twinning can help to satisfy the von Mises criterion, but it only contributes limited strain in a specific direction by complete reorientation of twins [8,9]. Therefore, the cutting-edge efforts to improve the formability of Mg alloys are to activate non-basal slips to provide more independent slip systems for arbitrary shape changes [7]. A likely solution would be deforming at elevated temperatures. Agnew et al. [10] have reported that the uniform elongation of AZ31 alloy could increase to ~45 % at 150 °C from ~13 % at RT. Lu et al. [11] found that plastic deformation of rolled magnesium alloy AZ31 would be more homogeneous at 150 °C compared with RT during compression along the normal direction (ND). The improvement of formability at higher temperatures, as shown above, emphasizes the crucial of a systematic and quantitative evaluation of the temperature dependence of the activation conditions of non-basal slip for optimizing hot working parameters.

The CRSS at various temperatures, as one of the most important parameters for the activation of non-basal slips in pure single crystal Mg, has been determined through tensile/compression testing along specific orientations that promote prismatic ⟨**a**⟩ slip [12–14] and pyramid ⟨**c + a**⟩ slip [15]. For example, Akhtar et al. [14] measured the temperature dependence of CRSS of prismatic slip in

* Corresponding authors.
E-mail addresses: zhangjiewang@mail.xjtu.edu.cn (Z.-J. Wang), zwshan@mail.xjtu.edu.cn (Z.-W. Shan).

https://doi.org/10.1016/j.jmst.2024.05.050
1005-0302/

single crystal Mg by conducting tensile testing along $<11\bar{2}0>$ direction to induce prismatic slip. The results showed that the CRSS of prismatic slip reduced from ~50 MPa at RT to ~25 MPa at 200 °C. Obara et al. [15] performed a compression test along the c-axis to activate pyramid ⟨**c + a**⟩ slip in single crystal Mg. The research showed that the CRSS of pyramid ⟨**c + a**⟩ slip decreased from ~40 MPa at RT to ~10 MPa at 300 °C. While for the most widely used commercial AZ31 alloy, the relevant studies are lacking for some reasons, possibly due to the challenge of obtaining bulk single-crystal samples.

The present studies of temperature effect on the activation of non-basal slip of AZ31 alloy primarily focus on testing in bulk polycrystalline materials and the determination of activation parameters of non-basal slip depends on experimental speculation [16–19]. The inevitable issue is that a discrepancy among these simulation results easily arises. One example is that Chapuis et al. [18] and Vaughan et al. [16] both indirectly fitted the activation of non-basal slip based on the stress-strain curves of AZ31 alloy with a similar grain size ~25 μm by visco-plastic self-consistent (VPSC) polycrystal modeling. By conducting simulations, their results showed that the CRSS of prismatic slip had a similar value, while pyramid ⟨**c + a**⟩ slip was quite different: ~250 MPa at RT decreased to ~60 MPa at 200 °C in Ref. [16] and ~210 MPa at RT decreased to ~150 MPa at 200 °C in Ref. [18]. Experimentally, Boehlert et al. [20] and Dessolier et al. [21] observed non-basal slip traces during in-situ tensile testing of AZ31 using a scanning electron microscope (SEM). They evaluated the contributions of non-basal slip to plastic deformation through a semi-quantitative analysis of counting slip traces. The slip trace analysis showed that the frequency of activated non-basal slips increased significantly from 50 to 300 °C. In any case, the temperature effects on the activation behavior of the non-basal slip of AZ31 alloy are still unknown.

In this study, we systematically investigated the plastic behaviors of AZ31 alloy from RT to 300 °C along ND using mechanical-thermal coupling depth-sensing nanoindentation. We quantitatively evaluated the activation shear stress of screw prismatic ⟨**a**⟩ slip. Furthermore, the activation of prismatic ⟨**a**⟩ dislocations exhibited abnormally enhanced displacement bursts, which could be characterized by Gaussian-like distribution rather than power-law statistics which have been extensively reported due to the destruction of jammed dislocation configurations.

2. Experiments and methods

2.1. Material preparation

The material used in the present study was hot-rolled AZ31 magnesium alloy that was annealed at 300 °C for 12 h under an Argon flow atmosphere to homogenize the microstructure. A specimen measuring 1.5 mm in thickness and having a horizontal plane of 4 mm × 5 mm was cut using electro-discharge machining, with the top surface oriented vertically to ND. The specimen surface was manually ground using abrasive SiC papers of 1200, 2400, 4000, and 7000 grit sizes, and then polished to a mirror finish with 0.5 μm alcohol-based diamond suspensions for 1 min. Afterward, the specimen was electropolished in an AC2 solution (800 mL ethanol + 100 mL propanol + 18.5 mL distilled water + 10 g hydroxyquinoline +75 g citric acid + 41.5 g sodium thiocyanate + 15 mL perchloric acid) at 20 V and −25 °C for 30 s to remove the entire remaining mechanical damage layer and for electron backscatter diffraction (EBSD) characterization. Final chemical etching was carried out in an ethanol-based solution (5 g trinitrophenol + 5 mL acetic acid + 10 mL deionized water + 100 mL ethanol) to reveal grain boundaries (GBs).

2.2. Mechanical testing at various temperatures

Instrumented nanoindentation tests were performed using a Hysitron Tribo-indenter TI950 with a Berkovich diamond indenter (tip radius R = 360 nm, calibrated by fitting the pure elastic loading segments on a standard fused quartz sample based on Hertzian contact theory). A binary device with top and bottom heating stages was used to heat the sample to the desired testing temperatures. Nitrogen gas was introduced around the sample as a protective measure to prevent oxidation of the sample surface. Indentations were made along ND with a maximum indentation load of 1000 μN and a holding time of 2 s. The loading and unloading rates were kept constant at 200 μN/s. The test temperatures were set to RT, 100, 150, 200, 250, and 300 °C at a heating rate of 50 °C/min. Before conducting the indentation test, the diamond tip was in contact with the sample surface for 20 s to ensure there was no temperature gradient between the tip and the sample and to control thermal drift to be less than 0.1 nm/s. For each of the testing temperatures, more than 100 indentations spaced at least 8 μm apart were made.

2.3. TEM characterization

For microstructural examination with transmission electron microscopy (TEM, JEM-2100), thin electron-transparent vertical cross-section samples containing pop-in indents were prepared using a focused ion beam (FIB, FEI Helios NanoLab 600 dual-beam) system. An ~1 μm thick protective layer of Pt was deposited on the indentation and then a slice of 20 μm × 5 μm × 2 μm was lifted out with FIB. The slice was FIB-thinned with a compensation angle of ± 2°. The FIB milling process was carried out symmetrically from both sides, with the ion beam current progressively decreased from 2.8 nA to 28 pA to minimize ion beam damage.

3. Results and discussion

3.1. Microstructure and texture of rolled AZ31 samples

Fig. 1 shows the microstructure of the starting materials. The inverse pole figure (IPF) (Fig. 1(a)) and the corresponding (0002) pole figure (Fig. 1(b)) maps show a typical strong basal texture with the c-axis in most grains closely aligned with ND. The grain size distribution (Fig. 1(c)) shows that the mean grain size is ~15 μm. The nanoindentation tests were performed on the large grains. The distinct GBs grooving can be clearly observed after the sample surface was chemically etched in an ethanol-based solution to precisely position the indentation within one grain (Fig. 1(d)).

The nanoindentation results at various temperatures are shown in Fig. 2. From RT to 250 °C, conspicuous displacement bursts are widely observed in the loading stage of P-h curves in Fig. 2(a) to Fig. 2(c). When the temperature rises to 300 °C, the P-h curve becomes rather smooth. Meanwhile, the creeping depth, specifically the increased depth during the holding stage (indicated by the blue arrowhead in Fig. 2(a–c)) steadily increases with rising temperature (as depicted in Fig. 2(d) of the blue curve). It coincides well with our general scenario that the higher the temperature, the better formability. For example, Xie et al. [22] conducted in situ compression tests on submicron aluminum pillars in TEM at various temperatures. The results showed that the sample exhibited a smoother stress-strain curve and improved formability at higher temperatures. However, surprisingly, when the temperature rises within the range of 150 to 250 °C, abnormally enhanced displacement bursts occur (indicated by the red arrows in Fig. 2(b, c)). These larger bursts, which deviate from the norm, lead to a non-monotonic change in the maximum burst size as temperature increases as shown in Fig. 2(d) of the red curve. The deformation

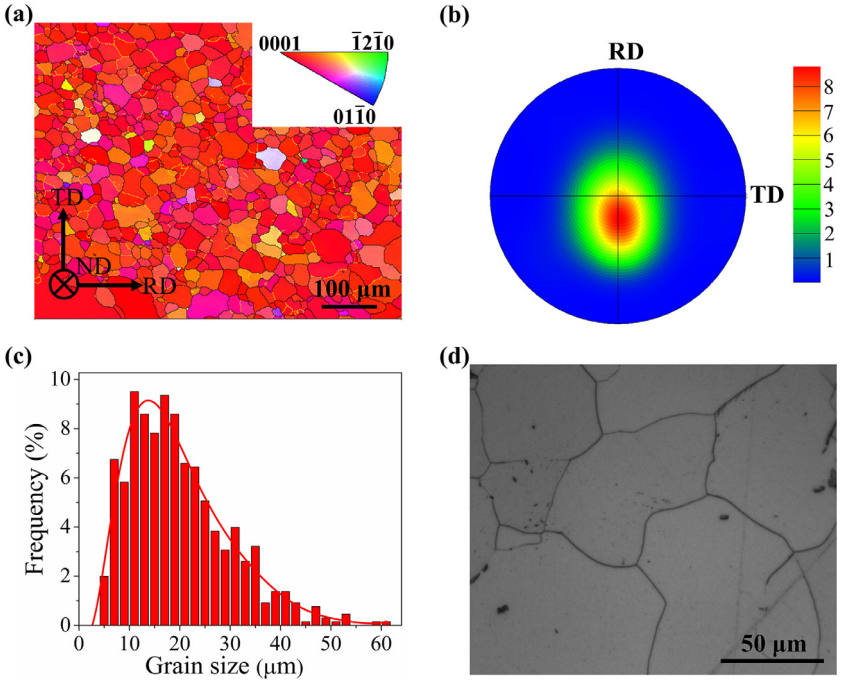

Fig. 1. The rolled AZ31 magnesium alloy exhibiting basal textures. (a) EBSD inverse pole figure (IPF) and (b) corresponding (0002) pole figure maps. (c) Grain size distribution shows that the mean grain size is ~15 μm. (d) GBs can be clearly observed after the final chemical etching in an ethanol-based solution.

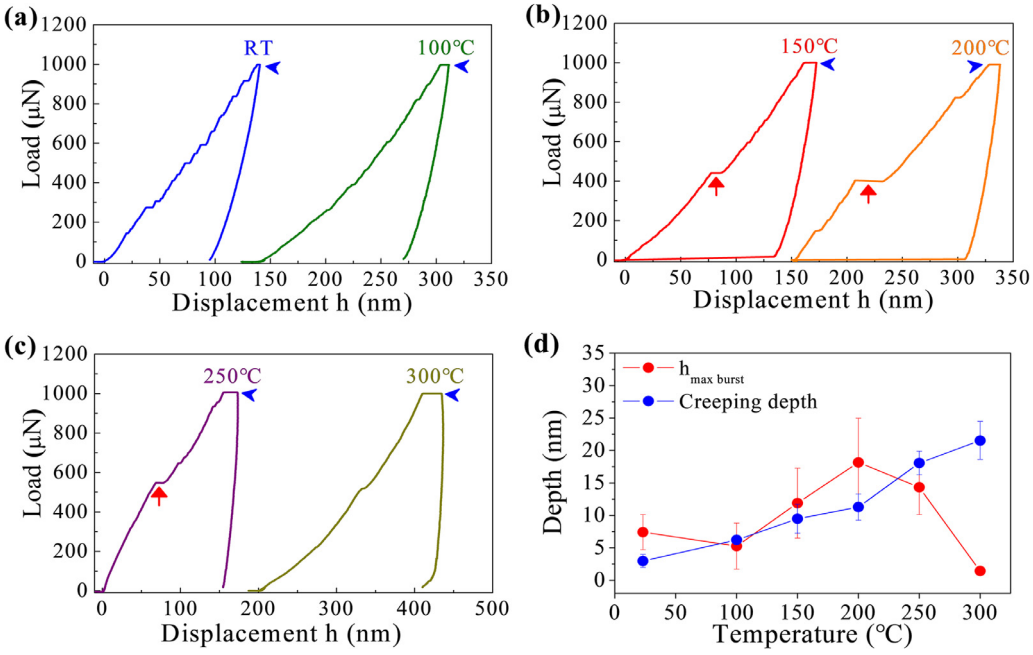

Fig. 2. Abnormally enhanced displacement bursts occurring at elevated temperatures ranging from 150 to 250 °C. (a–c) P-h curves at various temperatures. (d) The creeping depth increases monotonically with increasing temperature while the maximum displacement burst size Δh_{max} varies non-monotonically.

mechanism of such abnormal displacement bursts will be unveiled below.

3.2. The probability distribution of burst sizes

A quantitative statistical analysis of the burst sizes is beneficial in revealing their underlying physics. Fig. 3 shows the probability distribution of displacement burst sizes Δh at various temperatures (details on the specific data analysis process can be found in Fig. A.2 in Supplementary materials). At temperatures of RT and 100 °C (Fig. 3(a)), the displacement bursts can be solely characterized by power-law statistics with an exponent of ~1.5. These bursts, which satisfy a power law relationship, are considered to be associated with the collective, avalanche-like motion and reconstruction of dislocations [23]. However, in the temperature range of 150–250 °C (Fig. 3(b)), besides the power-law distribution, these abnormally enhanced displacement bursts (Fig. 2(b, c)) exhibit a Gaussian-like distribution (Fig. 3(b)), which implies an uncorrelated behavior of dislocations [24,25]. To uncover the specific physical mechanism behind these abnormally enhanced displacement

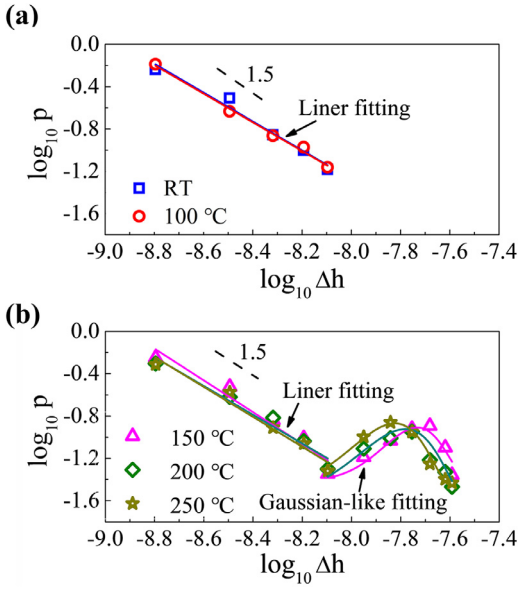

Fig. 3. The probability distribution of displacement burst magnitude Δh: (a) The bursts generated during RT to 100 °C can be characterized by power-law distribution and (b) while between 150 and 250 °C, besides the power-law distribution, the abnormally enhanced displacement bursts exhibit Gaussian-like distribution.

bursts, a thorough microstructure characterization beneath the indentations tested at RT and 250 °C is conducted using TEM below.

3.3. Transmission electron microscopy characterization

Fig. 4 shows the microstructure observed via TEM characterization beneath the indentation tested at RT. In the TEM bright-field image (Fig. 4(a)) with zone-axis of $[2\bar{1}\bar{1}0]$ and dark-field image with $\boldsymbol{g} = 01\bar{1}0$ (Fig. 4(b)), a deformed volume (outlined by a yellow dotted line) with a high density of tangled dislocations was developed just below the indentation. In contrast, after the indentation test at 250 °C, the region with densely tangled dislocations does not exist. Meanwhile, a dislocation array (indicated by the yellow arrow in Fig. 5(a)) parallel to the *c*-axis can be clearly observed beneath a newly formed, relatively clean grain (outlined by the yellow dotted line in Fig. 5(a)) which probably originates from dynamic recrystallization (DRX). The newly formed angle is ~0.26° calculated by $\tan\theta = b/d$, where d is the average spacing of dislocations in a dislocation array, b is the Burgers vector. The misorientation angle is too small to be distinguished in the diffraction pattern. Such a dislocation array has been extensively observed in the polycrystalline AZ31 alloy during hot deformation [26–29]. However, the mechanism behind it is still puzzling. As a comparison, another sample that has not yet exhibited the abnormally enhanced pop-in during testing at 250 °C was also characterized by TEM as shown in Fig. 6. It is obvious that the dislocation array does not exist beneath a similar shape of deformed volume (outlined by red dotted line in Fig. 6(b)). It should be noted that the deformed volume in Fig. 6(b) is not a grain. Within the deformed volume, it contains some tangled dislocations and a small newly formed grain outlined by the yellow dotted line in Fig. 6(b).

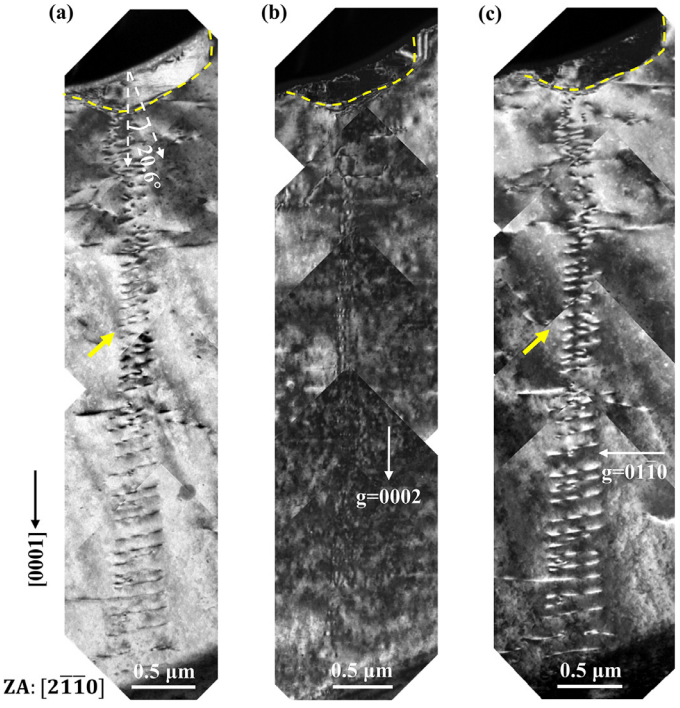

Fig. 5. TEM examination of the microstructure beneath the indentation conducted at 250 °C showing a dislocation array parallel to the c-axis emitted from GB. (a) Bright-field image. (b) Dislocation array is invisible under $\boldsymbol{g} = 0002$ condition and (c) visible under $\boldsymbol{g} = 01\bar{1}0$ condition.

To reveal the formation mechanism of the dislocation array, we analyze the specific Burgers vector of the dislocations in the array using the 2-beam weak beam dark-field ($\boldsymbol{g}/3\boldsymbol{g}$) technique. Based on the $\boldsymbol{g}\cdot\boldsymbol{b} = 0$ invisibility criterion as shown in Table 1, under the $\boldsymbol{g} = 0002$ condition, $\langle\mathbf{a}\rangle$ dislocation is invisible, while $\langle\mathbf{c}+\mathbf{a}\rangle$ dislocation is visible. Here, the dislocation array is invisible under $\boldsymbol{g} = 0002$ condition (Fig. 5(b)) and thus, the dislocations in the array are $\langle\mathbf{a}\rangle$ dislocations. In addition, the dislocation array is visible under $\boldsymbol{g} = 01\bar{1}0$ condition (Fig. 5(c)). Therefore, the Burgers vector of the dislocations is $\boldsymbol{b}_1 = \frac{a}{3}[1\bar{2}10]$ or $\boldsymbol{b}_2 = \frac{a}{3}[11\bar{2}0]$. To distinguish the specific Burgers vector ($\boldsymbol{b}_1$ or $\boldsymbol{b}_2$) through TEM imaging with a double-tilt holder is difficult because it needs to be tilted at a higher angle greater than 15°. The specific Burgers vector ($\boldsymbol{b}_1$ or $\boldsymbol{b}_2$) and type (screw or edge) of the dislocations will be determined

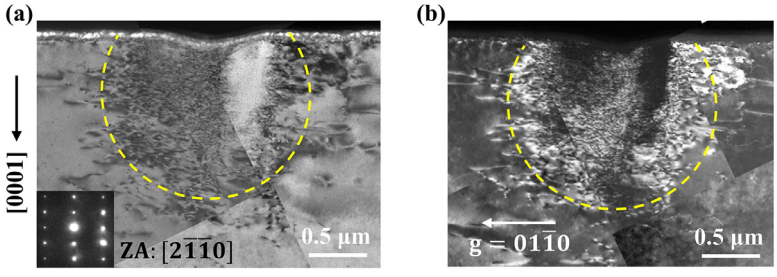

Fig. 4. TEM examination of the microstructure beneath the indentation conducted at RT showing a deformed region with high-density tangled dislocations. (a) Bright-field image and (b) dark-field image.

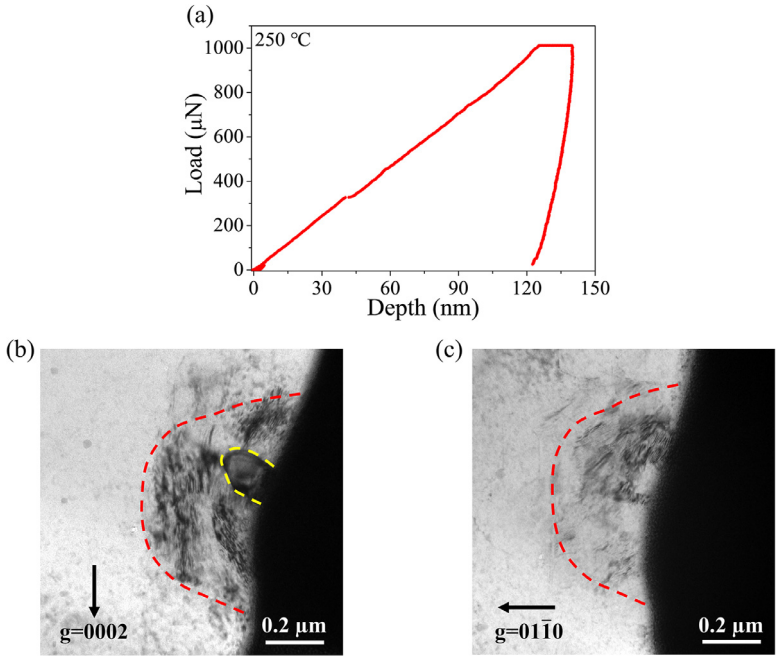

Fig. 6. TEM examination of the microstructure beneath the indentation that abnormally enhanced pop-in has not yet occurred during the indentation test at 250 °C. (a) *P–h* curve. (b) TEM image under $\boldsymbol{g} = 0002$ condition and (c) under $\boldsymbol{g} = 01\bar{1}0$ condition.

Table. 1
g*·*b analyses to determine the Burgers vector of dislocations.

$\boldsymbol{g}$	$\boldsymbol{b}$ ($\times\frac{a}{3}$)								
	$\pm[1\bar{2}10]$	$\pm[11\bar{2}0]$	$\pm[\bar{2}110]$	$[1\bar{2}13]$	$[1\bar{2}\bar{1}3]$	$[11\bar{2}3]$	$[11\bar{2}\bar{3}]$	$[\bar{2}113]$	$[\bar{2}11\bar{3}]$
0002	0	0	0	±2	∓2	±2	∓2	±2	∓2
$01\bar{1}0$	∓1	±1	0	∓1	∓1	±1	±1	0	0

by analyzing the geometric projective relationship of the sample in TEM.

Fig. 7(a–d) shows schematic diagrams illustrating the geometric projective diagram of four cases of dislocations in TEM with a zone-axis of $[2\bar{1}\bar{1}0]$. If the dislocation is edge cases and the blue solid lines $L1'$ (BG, Fig. 7(a)) and $L2'$ (FG, Fig. 7(b)) represent the projected image of dislocations with $\boldsymbol{b_1}$ and $\boldsymbol{b_2}$, then the corresponding actual dislocation lines would be L_1 (BD, Fig. 7(a)) and L_2 (FD, Fig. 7(b)) respectively. If the dislocation is screw case, the blue solid lines $L3'$ (FG, Fig. 7(c)) and $L4'$ (BG, Fig. 7(d)) are the projected images of the dislocation with $\boldsymbol{b_1}$ and $\boldsymbol{b_2}$, then L_3 (OF) and L_4 (OB) represent the corresponding actual dislocation lines respectively. Therefore, the actual length of the dislocation L_{dis} can be calculated using the following formula

$$L_{dis} = \kappa L_{proj} \tag{1}$$

where κ is 2 for the edge case and $2/\sqrt{3}$ for the screw case, L_{proj} is the observed projective length in TEM of the dislocation. Fig. 7(e) shows the diagram of the sample in a 3-dimensional coordinate system after a tilt operation to the zone-axis of $[\bar{2}110]$ along the *X*-axis with the angle of α and the *Y*-axis with the angle of β in the double-tilt holder coordinate system. When the sample tilts α degrees along the *X*-axis of the holder coordinate system, the initial direction of indentation, which is parallel to the normal direction of the sample's upper surface $\overrightarrow{OP_0}$, tilts to $\overrightarrow{OP}$ with the angle of α along the *x-z* plane in the 3-dimensional coordinate system. When the sample tilts β degrees along the *Y*-axis of the holder coordinates, the indentation direction does not change. Meanwhile, during the tilting operation, the normal direction of the side face of the sample $\overrightarrow{OQ_0}$, which is parallel to the direction of the sample thickness, tilts to $\overrightarrow{OQ}$ with the angle of γ in the 3-dimensional coordinate system. After performing the tilt operation, the angle ε, between the *c*-axis (parallel to $\overrightarrow{OC}$) and the projective direction of the indentation direction in *y-z* plane (parallel to $\overrightarrow{OP_0}$), can be directly measured in TEM. To simplify the calculation, the magnitude of the vector $\overrightarrow{OC}$, $\overrightarrow{ON}$ (parallel to $\boldsymbol{b_1}$), $\overrightarrow{OM}$ (parallel to $\boldsymbol{b_2}$), $\overrightarrow{OP}$ and $\overrightarrow{OQ}$ is set to 1. Then the coordinates of these vectors in the 3-dimensional coordinate system are: $\overrightarrow{OC}$ = (0, sin(ε), −cos(ε)), $\overrightarrow{ON}$ = (sin30°, −cos30°cos(ε), −cos30°sin(ε)), $\overrightarrow{OM}$ = (sin30°, cos30°cos(ε), cos30°sin(ε)), $\overrightarrow{OP}$ = (sin(α), 0, −cos(α)), $\overrightarrow{OQ}$ = (cos(α)cos(β), sin(β), sin(α)cos(β)). Similarly, as shown in Fig. 7(a–d), the vector coordinates in the direction of the four kinds of dislocation line length are: $\overrightarrow{BD}$ = (sin60°, cos60°cos(ε), cos60°sin(ε)), $\overrightarrow{FD}$ = (sin60°, −cos60°cos(ε), −cos60°sin(ε)), $\overrightarrow{FO}$ = (sin30°, -cos30°cos(ε), -cos30°sin(ε)), $\overrightarrow{BO}$ = (sin30°, cos30°cos(ε), cos30°sin(ε)). The relationship between the length of the dislocation line and the thickness of the sample can be expressed by the following formula

$$T = L_{dis}\cos(\delta) \tag{2}$$

where T is the thickness of the sample, δ is the angle between the direction of the normal direction of the side face of the sample ($\overrightarrow{OQ}$) and the direction of the dislocation line ($\overrightarrow{BD}$, $\overrightarrow{FD}$, $\overrightarrow{FO}$, or $\overrightarrow{BO}$) and can be calculated using vector calculation. For the sample in Fig. 5, α is ∼−4.6°, β is ∼4.4°, and ε is ∼20.6°, the projected length of the dislocation line L_{proj} in Fig. 5(a) is approximately 270–440 nm, then for the four cases of the dislocations in Fig. 7(a–d), the calculated thickness of the sample T is approximately 444–

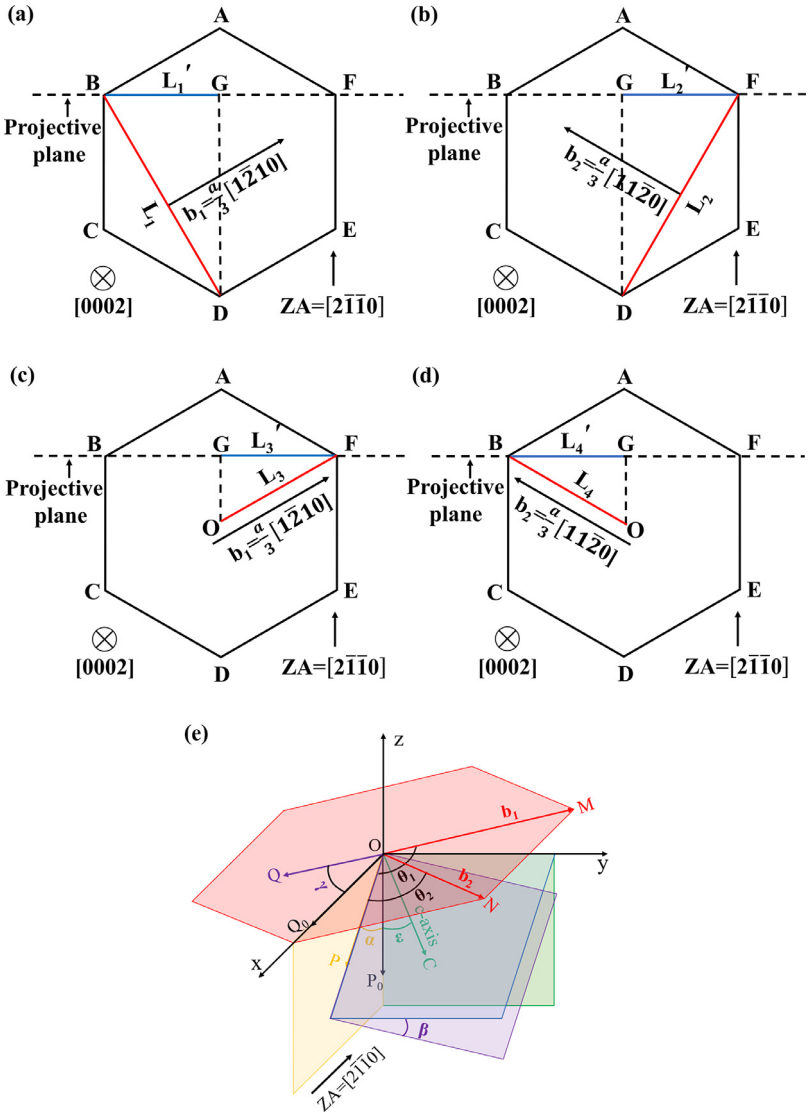

Fig. 7. Schematic diagrams illustrating the geometric projective diagram in TEM of four cases of dislocations in the projective plane. (a, b) Edge dislocation. (c, d) Screw dislocation. (e) The projective diagram in three-dimensional coordinates after the tilt operation of the sample in TEM with a double-tilt holder.

724, 456–742, 143–236, and 167–271 nm respectively. Considering the measured thickness of our sample by FIB is ~262 nm (outlined by a red solid line as shown in Fig. A.1(a)), the dislocation should be of the screw type with $\boldsymbol{b_2}$.

If the abnormally enhanced bursts originate from the observed screw ⟨**a**⟩ dislocation array, the number of dislocations in the array can be determined by displacement burst magnitude using the formula

$$n = \frac{\Delta h}{b\cos\theta} \tag{3}$$

where n is the calculated number of dislocations in the array, Δh is the magnitude of the displacement burst which can be estimated by observing the sudden change in the displacement rate, as shown in Fig. A.3, b is the magnitude of $\boldsymbol{b}$, θ is the angle between the indentation direction (parallel to $\overrightarrow{OP}$) and $\boldsymbol{b}$ ($\boldsymbol{b_1}$ or $\boldsymbol{b_2}$) and can be calculated using vector calculation.

For quantitative analysis of the relationship between the dislocation array and the abnormally enhanced displacement burst, we conducted an indentation test at 250 °C near a GB to expect that the movement of the dislocation array can be hindered by a pre-existing GB. The indentation is ~4.6 μm away from GB which is large enough to exclude the effect of GB on pop-in behavior. In this test, the loading process terminated almost immediately after the burst. As shown in Fig. 8(a), a dislocation array can also be observed, and a GB exists in front of the dislocation array (indicated by a white arrow in the bottom left corner in Fig. 8(a)). It is worth noting that, unlike the sample in Fig. 5, this dislocation array appears to be emitted from the contact interface between the sample and the indenter. The dislocation array is also invisible under $\boldsymbol{g}$ = 0002 condition (Fig. 8(b)) and visible under $\boldsymbol{g}$ = 01$\bar{1}$0 condition (Fig. 8(c)). Using Eqs. (1) and (2), the calculated thickness of the sample T for the four cases of the dislocations is ~115, ~151, ~26, and ~62 nm respectively ($L_{\text{proj}} \approx$ 20.8 nm, the sample thickness T is ~67 nm as shown in Fig. A.1(b) outlined by a red solid line), therefore, the dislocation is also determined to be of the screw type with $\boldsymbol{b_2}$. Using Eq. (3), the calculated dislocations are ~105 (α = –6.2°, β = 15.7°, ε = 40.8°, $\theta \approx$ 51.9°, $\Delta h \approx$ 20.8 nm), which is slightly larger than that observed in TEM (~100). Considering that dislocations near the surface can escape out of the sample due to the surface image forces, the calculated result still fits perfectly. The activated dislocations with Burgers vector $\boldsymbol{b_2}$ not $\boldsymbol{b_1}$ may be rationalized by the fact that the Schmidt factor m of $\boldsymbol{b_2}$ is larger than $\boldsymbol{b_1}$ for both of the two samples (for

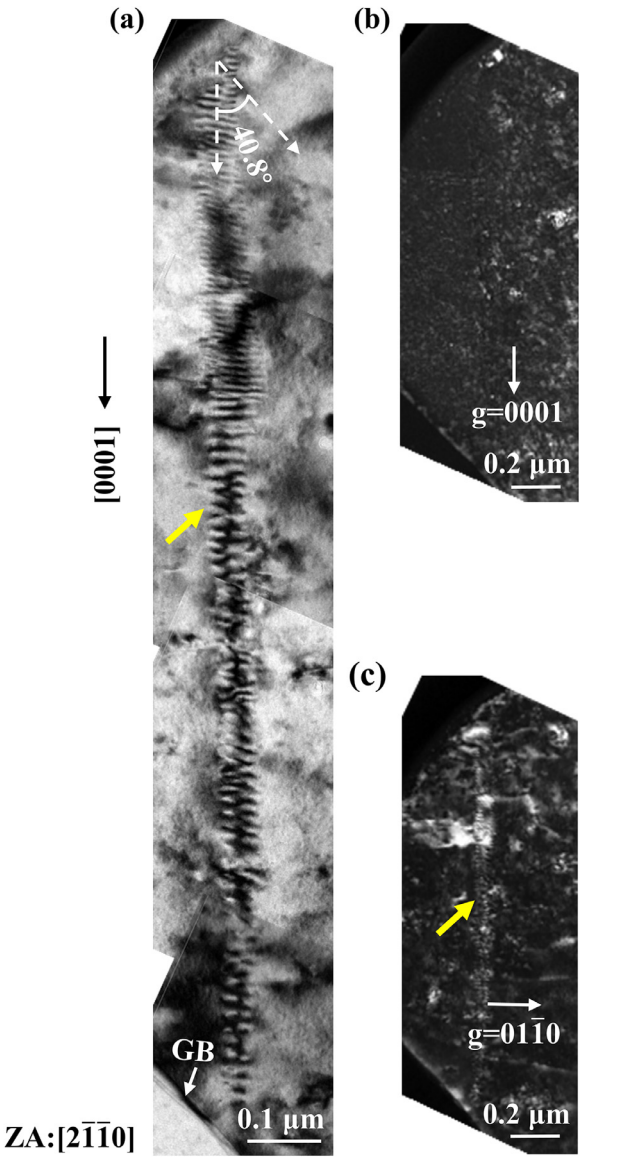

Fig. 8. TEM examination of microstructure beneath another indentation conducted near GB at 250 °C showing dislocation array parallel to the *c*-axis emitted from the contact interface between the sample and the indenter: (a) The bright-field image. (b) Dislocation array is invisible under $\boldsymbol{g}$ = 0002 condition and (c) visible under $\boldsymbol{g}$ = 01$\bar{1}$0 condition.

sample in Fig. 5: m_1 = 0.248, m_2 = 0.321; for sample in Fig. 8: m_1 = 0.391, m_2 = 0.46). Therefore, the abnormally enhanced displacement bursts originate exactly from the formation of prismatic screw ⟨**a**⟩ dislocation array.

3.4. Heterogeneous dislocation nucleation

Next, we will explore the formation mechanism of the dislocation array by evaluating the activation stress and activation volume due to that the specific mechanism often exhibits significant differences in activation parameters [30–33].

During the plastic deformation stage, the indentation hardness when a burst occurs can be calculated using the formula

$$H = \frac{P}{A_c} \tag{4}$$

where P is the loading force, and A_c is the contact area which can be estimated by functions of the contact area and indentation depth established using an atomic force microscope (AFM) (as shown in Fig. A.4). Then the equivalent flow stress can be estimated using the following empirical formula

$$\sigma = \frac{1}{3}H \tag{5}$$

where σ is the equivalent flow stress. With σ, the maximum shear stress can be calculated based on the von Mises yield criterion using the formula

$$\tau = \frac{\sqrt{3}}{3}\sigma \tag{6}$$

where τ is the maximum shear stress beneath the indentation. The method has been referenced in Ref. [37]. Fig. 9(a) shows the cumulative probability, f, of the calculated activation stress at various temperatures. The calculated activation stress (about G/26–G/14 at 150 °C, G/24–G/13 at 200 °C, and G/31/–G/15 at 250 °C, G is the shear modulus at the corresponding temperatures [34]) is at the lower limited of theoretical shear strength for metals (G/30–G/5) [32]. The cumulative probability can also be correlated with the maximum shear stress using the following expression [35]

$$f = 1 - \exp\left[\frac{-\eta KT}{\tau \nu^*}\exp\left(\frac{\tau \nu^*}{KT}\right)\right] \tag{7}$$

where η is the attempt frequency for the yield stress which can be interpreted as the maximum shear stress τ, and ν^* is the activation volume. By plotting ln[–ln(1–f)] vs. the shear stress τ as shown in Fig. 9(b), the experimental data is found to fall onto approximately linear lines. With the slope of the fitted curves, the activation volume of these abnormally enhanced bursts, calculated using Eq. (5), is deduced to be $\sim 3b^3$. Therefore, considering the high activation stress and the small activation volume, the formation mechanism of the dislocation array is dominated by the heterogeneous nucleation of prismatic screw ⟨**a**⟩ dislocations from the GB (Fig. 5) or the contact interface (Fig. 8).

Recently, Sato et al. [36] also reported Gaussian-like statistics from dislocation nucleation during nanoindentation on single crystal Fe and Cu. The difference is that, in their research, dislocation nucleation correlates with the onset of plasticity, namely the first displacement burst. It is worth noting that in addition to the Gaussian-like statistics from prismatic ⟨**a**⟩ dislocations nucleation, there still is power-law distribution at temperatures between 150 and 250 °C in Fig. 3(b). For these data points, we propose that it also arises from the destruction of jammed dislocation configurations within the deformed volume (as shown in Fig. 6(b)), albeit fewer than at RT (as shown in Fig. 4). The tangled dislocation structure is easily depinned and vanishes due to dynamic recovery and dynamic recrystallization (as shown in Figs. 5(a) and 6(b) outlined by yellow dotted line) at higher temperatures (0.46 T_m to 0.57 T_m) during the subsequent deformation. When dislocation starvation occurs and diffusive plasticity cannot satisfy the imposed plastic strain, dislocation nucleation characterized by abnormally enhanced pop-ins occurs to accommodate further plastic deformation. In addition, the activation stress for prismatic and basal slip of Mg exhibits a significant decrease in anisotropy with increasing temperature [12,19]. Therefore, we observed the activation of prismatic ⟨**a**⟩ slip. Additional simulations on an atomic scale and experiments will be needed to uncover the activation process and the contribution to subsequent plastic deformation of the prismatic screw ⟨**a**⟩ dislocation array.

4. Summary

In summary, the effects of temperature on the plastic deformation behaviors of AZ31 magnesium were systematically investigated from RT to 300 °C by nanoindentation. Besides the well-reported displacement bursts with power-law scaling between the

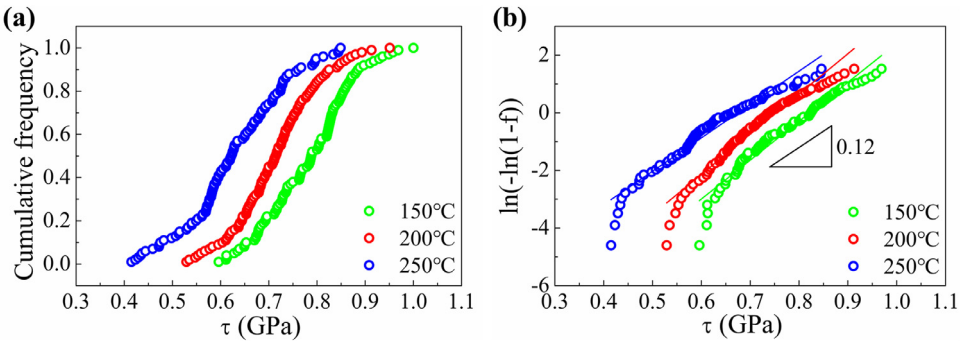

Fig. 9. The statistics of the maximum indentation shear stress. (a) The cumulative frequency of the maximum indentation shear stress. (b) Extracting the activation volume by a linear fitting procedure of ln[−ln(1−*f*)] vs. τ.

numbers of events and their magnitude, abnormally enhanced displacement bursts characterized by Gaussian-like statistics existed at elevated temperatures ranging from 150 to 250 °C. By conducting a detailed examination of the microstructure beneath the indentation using TEM, we demonstrated that the abnormal bursts originated from the heterogeneous nucleation of a prismatic screw ⟨**a**⟩ dislocation array from GB or contact interface. The abnormally enhanced burst can degrade the inherent structural properties and make precision shaping challenging.

Declaration of competing interest

The authors declare that they have no known competing financial interests or personal relationships that could have appeared to influence the work reported in this paper.

CRediT authorship contribution statement

Song-Yu Yan: Writing – review & editing, Writing – original draft. **Zhang-Jie Wang:** Writing – review & editing. **Zhi-Wei Shan:** Writing – review & editing, Supervision, Project administration.

Acknowledgements

This work was supported by the Natural Science Foundation of China (Nos. 52031011 and 51971167). We acknowledge Yuan-Bin Qin and Dan-Li Zhang (Xi'an Jiaotong University) for assistance in Nanoindentation and TEM experiments.

Supplementary materials

Supplementary material associated with this article can be found, in the online version, at doi:10.1016/j.jmst.2024.05.050.

References

[1] A.A. Luo, J. Magnes. Alloy. 1 (2013) 2–22.
[2] Z. Yang, J.P. Li, J.X. Zhang, G.W. Lorimer, J. Robson, Acta Metall. Sin. (Engl. Lett.) 21 (2008) 313–328.
[3] Q.Y. Li, G.F. Jiang, J. Dong, J.W. Hou, G. He, J. Alloy. Compd. 680 (2016) 522–530.
[4] T. Mukai, H. Watanabe, K. Higashi, Mater. Sci. Technol. 16 (2000) 1314–1319.
[5] W.P. Jia, X.D. Hu, H.Y. Zhao, D.Y. Ju, D.L. Chen, J. Alloy. Compd. 645 (2015) 70–77.
[6] G.W. Groves, A. Kelly, Philos. Mag. 8 (1963) 877–887.
[7] W.W. Hu, Z.Q. Yang, H.Q. Ye, Acta Mater. 124 (2017) 11.
[8] X. Lou, M. Li, R.K. Boger, S.R. Agnew, R.H. Wagoner, Int. J. Plast. 23 (2007) 44–86.
[9] B. Li, X.Y. Zhang, Scr. Mater. 71 (2014) 45–48.
[10] S.R. Agnew, Ö. Duygulu, Int. J. Plast. 21 (2005) 1161–1193.
[11] L. Lu, B.X. Bie, Q.H. Li, T. Sun, K. Fezzaa, X.L. Gong, S.N. Luo, Acta Mater. 132 (2017) 389–394.
[12] G.D. Sim, K.Y. Xie, K.J. Hemker, J.A. El-Awady, Acta Mater. 178 (2019) 8.
[13] N.M. della Ventura, P. Schweizer, A. Sharma, M. Jain, T.E.J. Edwards, J.J. Schwiedrzik, C. Peruzzi, R.E. Logé, J. Michler, X. Maeder, Acta Mater. 243 (2023) 118528.
[14] A. Akhtar, E. Teghtsoonian, Acta Metall. 17 (1969) 1351–1356.
[15] T. Obara, H. Yoshing, S. Morozumi, Acta Metall. 21 (1973) 845–853.
[16] M.W. Vaughan, W. Nasim, E. Dogan, J.S. Herrington, G. Proust, A.A. Benzerga, I. Karaman, Acta Mater. 168 (2019) 448–472.
[17] A. Jain, S.R. Agnew, Mater. Sci. Eng. A 462 (2007) 8.
[18] A. Chapuis, Q. Liu, Mater. Sci. Eng. A 725 (2018) 108–118.
[19] M.R. Barnett, Metall. Mater. Trans. A 34 (2003) 1799–1806.
[20] C.J. Boehlert, Z. Chen, I. Gutiérrez-Urrutia, J. Llorca, M.T. Pérez-Prado, Acta Mater. 60 (2012) 1889–1904.
[21] T. Dessolier, P. Lhuissier, F. Roussel-Dherbey, F. Charlot, C. Josserond, J.J. Blandin, G. Martin, Mater. Sci. Eng. A 775 (2020) 138957.
[22] D.G. Xie, R.R. Zhang, Z.Y. Nie, J. Li, E. Ma, J. Li, Z.W. Shan, Acta Mater. 188 (2020) 570–578.
[23] F.F. Csikor, C. Motz, D. Weygand, M. Zaiser, S. Zapperi, Science 318 (2007) 251–254.
[24] J. Weiss, W. Ben Rhouma, T. Richeton, S. Dechanel, F. Louchet, L. Truskinovsky, Phys. Rev. Lett. 114 (2015) 105504.
[25] P. Zhang, O.U. Salman, J.Y. Zhang, G. Liu, J. Weiss, L. Truskinovsky, J. Sun, Acta Mater. 128 (2017) 351–364.
[26] M.M. Myshlyaev, H.J. McQueen, A. Mwembela, E. Konoplev, Mater. Sci. Eng. A 337 (2002) 13.
[27] J.C. Tan, M.J. Tan, Mater. Sci. Eng. A 339 (2003) 9.
[28] J.W. Liu, Z.H. Chen, G.F. Li, T. Nonferr, Metal. Soc. 22 (2012) 1329–1335.
[29] H.W. Son, J.W. Lee, S.K. Hyun, Int. J. Plast. 125 (2020) 118–132.
[30] J.K. Mason, A.C. Lund, C.A. Schuh, Phys. Rev. B 73 (2006) 054102.
[31] Z.G. Wang, H. Bei, E.P. George, G.M. Pharr, Scr. Mater. 65 (2011) 469–472.
[32] C. Zhu, Z.P. Lu, T.G. Nieh, Acta Mater. 61 (2013) 2993–3001.
[33] D. Catoor, Y.F. Gao, J. Geng, M.J.N.V. Prasad, E.G. Herbert, K.S. Kumar, G.M. Pharr, E.P. George, Acta Mater. 61 (2013) 2953–2965.
[34] H. Somekawa, K. Hirai, H. Watanabe, Y. Takigawa, K. Higashi, Mater. Sci. Eng. A 407 (2005) 53–61.
[35] C.A. Schuh, A.C. Lund, J. Mater. Res. 19 (2004) 2152–2158.
[36] Y. Sato, S. Shinzato, T. Ohmura, T. Hatano, S. Ogata, Nat. Commun. 11 (2020) 4177.
[37] W.D. Nix, H.J. Gao, J. Mech. Phys. Solids 46 (1998) 411–425.